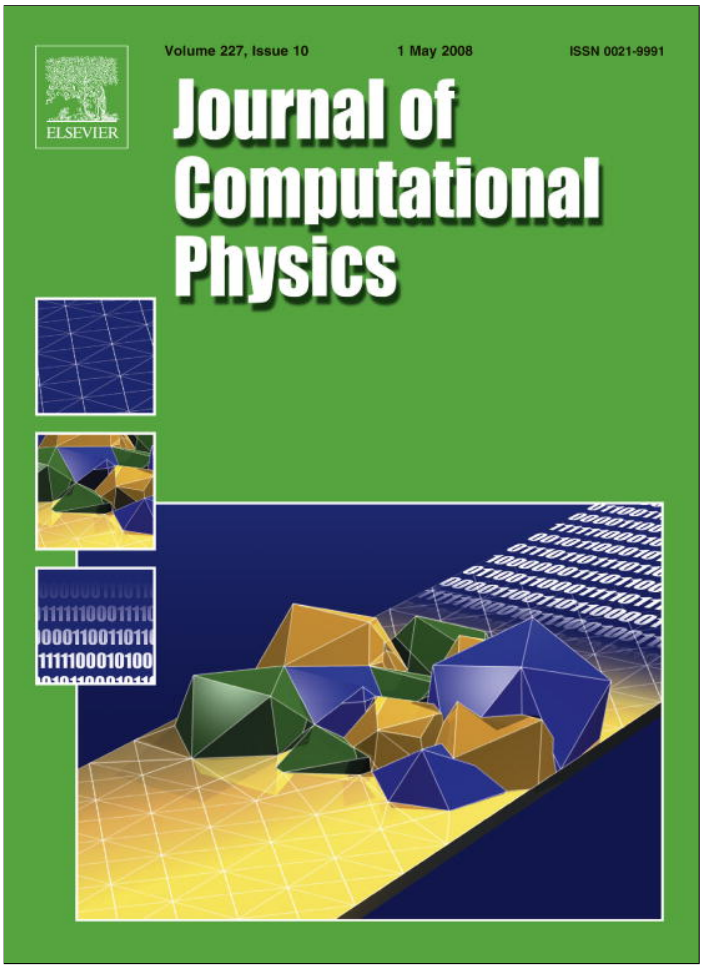

Available online at www.sciencedirect.com
ScienceDirect
Journal of Computational Physics 227 (2008) 4998–5018
JOURNAL OF COMPUTATIONAL PHYSICS
www.elsevier.com/locate/jcp

Front tracking simulation of deformation and buckling instability of a liquid capsule enclosed by an elastic membrane

Xiaoyi Li, Kausik Sarkar *

Department of Mechanical Engineering, University of Delaware, Newark, DE 19716, United States

Received 12 March 2007; received in revised form 11 January 2008; accepted 17 January 2008
Available online 2 February 2008

Abstract

The dynamics of a liquid capsule enclosed by an elastic membrane in a shear flow is investigated using a front tracking finite difference method. We compute deformation, orientation and tank-treading of the capsule, as functions of the forcing (capillary number) and the viscosity ratio for two different membrane constitutive equations – Neo-Hookean and Skalak. The computed results compare very well with those obtained by high-order boundary element methods as well as the small deformation perturbation analysis. The simulation shows that a drop and a capsule, even under those circumstances that result in the same Taylor deformation criterion for both, attain very different shapes. The tank-treading period even for different capillary numbers as well as capsules with different constitutive laws, is primarily determined by the deformation and the viscosity ratio. At low capillary numbers the simulation predicts buckling due to large compressive stresses on the membrane. However, we show that in shear, unlike in extension, the tank-treading motion can inhibit the buckling instability and gives rise to a stable evolution even in presence of membrane compressive stresses. At large capillary numbers the capsule experiences large bounded shape followed by tip buckling indicating possible membrane breakup.

Keywords: Front tracking; Elastic membrane; Deformation; Tank-treading; Buckling instability; Breakup

1. Introduction

The membrane of a biological cell comprises of a lipid bilayer supported by a network of trans-membrane proteins that gives rise to an elastic property for the membrane. Synthetic capsules with elastic polymerized membranes also have important applications in many biomedical processes such as drug delivery and artificial-organ manufacturing. As a result, much effort has been devoted to understand the dynamics of elastic capsules in well defined flows. The first theoretical study of elastic capsules was conducted by Barthès-Biesel [1] and Barthès-Biesel and Rallison [2] using a perturbation method for small capsule deformation. Subsequently,

* Corresponding author. Tel.: +1 302 831 0149.
E-mail address: sarkar@me.udel.edu (K. Sarkar).

0021-9991/$ - see front matter © 2008 Elsevier Inc. All rights reserved.
doi:10.1016/j.jcp.2008.01.034

a number of simulation studies have been executed to investigate large deformation and breakup of capsules. Most of these studies were performed using the boundary element method (BEM), which is limited to the inertia-less Stokes flow of a viscous fluid. However, capsule dynamics in real life applications could arise with additional complexities – both the membrane and the bulk fluid might be viscoelastic for biological systems. The processing flows in many industries are turbulent with inertia and fluctuations. Finite inertia, viscoelasticity and other complexities motivate the present study to evaluate the capability of an alternative to BEM. We investigate the capsule dynamics in a steady shear flow using a front tracking finite difference method [3]. We carefully investigate our results vis-à-vis those of previous BEM investigations giving special attention to issues such as criteria for membrane instabilities and failure.

In the past, a number of different membrane constitutive equations have been used to describe the membrane response. Kraus et al. [4] simulated steady tank-treading motion [5] of an area-incompressible membrane with a finite bending rigidity in shear, and predicted the tank-treading frequency (TTF) to be proportional to the shear rate. Navot [6] used a network of connected springs to model the polymeric membrane, and found bounded deformation at large shear rates.

Pozrikidis [7] and Ramanujan and Pozrikidis [8] modeled the membrane using the so called zero-thickness shell, and showed its equivalence to the Neo-Hookean model in predicting capsule deformation. They investigated breakup of capsules in shear [7] with simulations using a structured curvilinear coordinate to describe the membrane. Based on previous experimental observations [9], the authors suggested two possible failure mechanisms: membrane thinning and excessive tension, both of which occurring at the same location near the capsule tip. They argued that the location of membrane failure therefore might be insensitive to the precise rupture mechanism. Ramanujan and Pozrikidis [8] adopted an unstructured triangular discretization to remove the numerical instability due to uneven discretization in the curvilinear system. Using such a discretization, the authors were able to obtain stable bounded capsule deformation even at high shear rates. We note that a compressive stress was found at the high-curvature tips of largely deformed capsules in their numerical results [8, Fig. 8], which assumes importance in the current study specially in view of the later investigation by Barthès-Biesel and co-workers (see below). The compressive stress near the capsule tips can cause buckling and induce membrane failure.

Barthès-Biesel and co-workers [10,11] used a structured discretization of the membrane. They investigated deformation of a spherical capsule with a higher order BEM, and therefore with a more accurate computation of surface geometry than has been achieved before. They found compressive stresses at both low and high capillary numbers, and stated that compressive stress directly causes the membrane to be unstable and to develop numerical (unphysical) buckles in the absence of bending rigidity [10]. The authors numerically identified an interval of capillary numbers for each particular flow and membrane constitutive law where the stress is tensile everywhere on the membrane, and therefore the capsule can achieve a stable shape. Outside the interval, they found that the membrane develops compressive stresses and becomes unstable by a mechanism similar to that of Euler buckling. In a subsequent work, they imposed an isotropic tensile prestress [12] on the membrane in order to overcome the destabilizing effects of compressive stress. We note that the stability of a membrane surrounded by a viscous fluid is affected not only by the stresses on the membrane, but also by its motion (e.g. tank-treading). It should be noted that although a qualitative comparison between simulations and experiments [9,13] has been obtained, a quantitative criterion for capsule instability and buckling is currently not available.

There are other grid-based immersed interface methods, such as volume of fluid [14], level set [15] and phase field [16], which offer similar advantages over boundary elements in handling multiphase flows with moving boundaries. They along with front tracking have been used to investigate effects of inertia [17–21] and viscoelasticity [22–28] on drops characterized by isotropic surface tension. Rheology of an emulsion of such drops at finite inertia has also been studied [29–32]. However, much less attention has been paid to modeling elastic capsules using such methods. One exception was the modeling of red blood cells by Eggleton and Popel [33] using a front tracking method (FT). Recently, FT is used to simulate two-dimensional capsules [34]. Compared to other immersed interface methods, FT utilizes a separate mesh to describe the membrane, which allows easy tracking of deformation history for calculating elastic forces. Limited by computational costs, Eggleton and Popel's simulation was conducted on a coarse discretization for short periods of time. Effects of viscosity ratio between the dispersed and continuous fluids were not considered. In view of its widespread

use, a careful analysis of the limitations and the capability of front tracking is in order. One also needs to understand how the method treats capsule instabilities due to membrane compression and breakup.

Working towards this goal, in the present study we implement various membrane constitutive models used in previous boundary element investigations. We examine the effects of different constitutive laws and viscosity ratio on capsule behavior, and compare our front tracking predictions of capsule with those obtained by BEM. Further extensions to cases with high inertia and fluid viscoelasticity are feasible, but not considered here. In the following, we first describe the front tracking formulation and the numerical algorithm for adding the elastic membrane force. Then we discuss the simulation results for a spherical capsule in shear at low Reynolds number. We investigate the numerical accuracy of our front tracking simulation. Capsules with different membrane types and different ratios of dispersed to continuous fluid viscosities are simulated and compared with similar results by BEM. The issues regarding bucking instability and breakup are also explored and discussed in the context of earlier findings by BEMs.

2. Formulation

2.1. Governing equations

We consider the fluid inside the capsule and outside to be Newtonian; the flow is governed by the continuity and Navier–Stokes equations:

$$\begin{aligned} &\nabla \cdot \mathbf{u} = 0, \\ &\frac{\partial(\rho \mathbf{u})}{\partial t} + \nabla \cdot (\rho \mathbf{u}\mathbf{u}) = -\nabla p + \nabla \cdot [\mu\{\nabla \mathbf{u} + (\nabla \mathbf{u})^{\mathrm{T}}\}] - \int_{\partial B} \mathbf{f}^{\mathrm{m}}(\mathbf{x}')\delta(\mathbf{x} - \mathbf{x}')\mathrm{d}S(\mathbf{x}'), \end{aligned} \tag{1}$$

where p is the pressure, ρ the density and μ the viscosity of the fluid. The density and viscosity are uniform in each phase and are allowed to have a sharp variation across the membrane ∂B separating them. In this work, the capsules are assumed to be neutrally buoyant with same density as that of the liquid outside. The superscript T represents transpose. $\mathbf{f}^{\mathrm{m}}$ is the surface traction in the membrane arising as a jump in the stress condition across the membrane. The surface membrane force is written as a singular volume

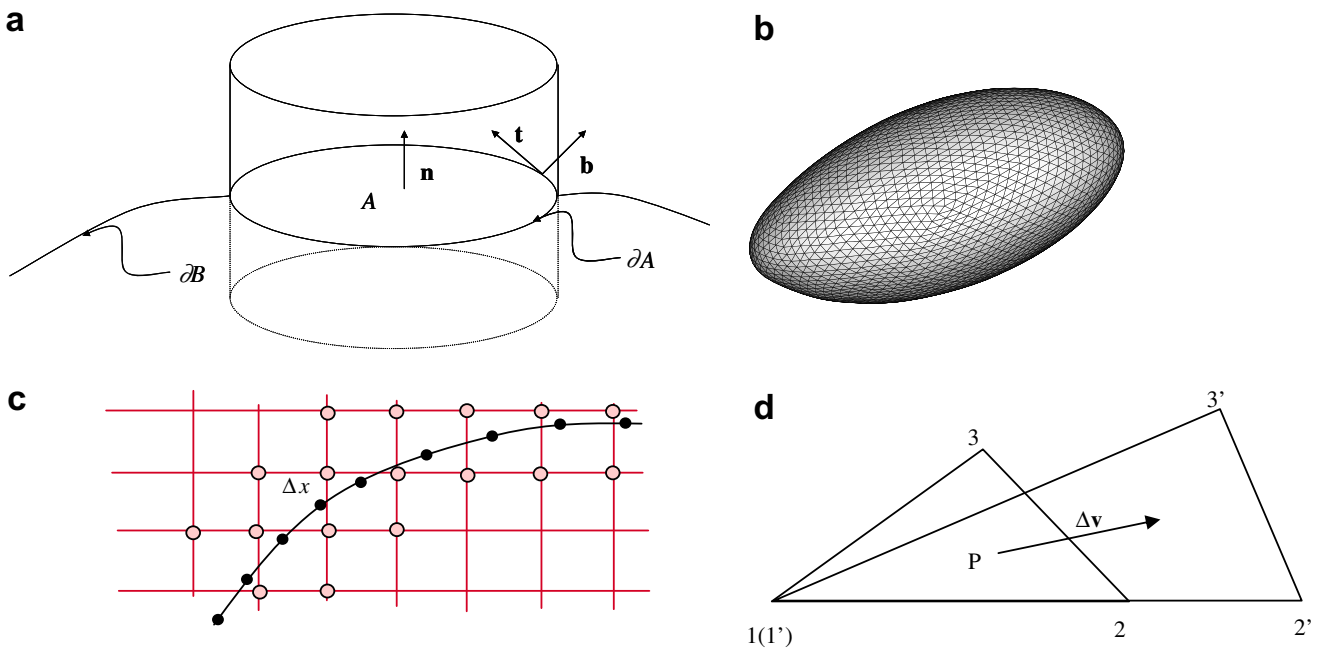

Fig. 1. (a) Geometry of the surface and pillbox; (b) an unstructured triangular mesh is used to discretize the membrane; (c) the sharp membrane interface is smeared over a few neighboring grid points; (d) undeformed triangle element 123 and deformed triangle element $1'2'3'$ in the same local coordinate.

force using Dirac delta function $\delta(\mathbf{x}-\mathbf{x}')$; the force is present only at the boundary. We note that the single-fluid formulation (1) is completely equivalent to the conventional description involving separate equations in each domain with kinematic and dynamic conditions at the interface. Specifically, the jump condition at the membrane interface is obtained by considering momentum conservation in a pillbox straddling the membrane (Fig. 1a). In the limit of pillbox thickness across the membrane going to zero, momentum conservation takes the following form:

$$\begin{aligned}\int_A (\boldsymbol{\sigma}^{(\mathrm{d})}-\boldsymbol{\sigma}^{(\mathrm{c})})\cdot\mathbf{n}\,\mathrm{d}S &= -\int_{\partial A}\boldsymbol{\tau}^{\mathrm{m}}\cdot\mathbf{b}\,\mathrm{d}C = -\int_{\partial A}\boldsymbol{\tau}^{\mathrm{m}}\cdot(\mathbf{t}\times\mathbf{n})\mathrm{d}C = \int_A \nabla^{\mathrm{s}}\cdot\boldsymbol{\tau}^{\mathrm{m}}\,\mathrm{d}S \\ &= -\int_A \mathbf{f}^{\mathrm{m}}\,\mathrm{d}S \Longleftrightarrow [\boldsymbol{\sigma}^{(\mathrm{d})}(\mathbf{x}_B)-\boldsymbol{\sigma}^{(\mathrm{c})}(\mathbf{x}_B)]\cdot\mathbf{n} = -\mathbf{f}^{\mathrm{m}}(\mathbf{x}_B), \quad \mathbf{x}_B\in\partial B,\end{aligned} \tag{2}$$

where, $\boldsymbol{\sigma}^{(\mathrm{d})}$ and $\boldsymbol{\sigma}^{(\mathrm{c})}$ are the stress in the fluid inside and outside the capsule, and $\mathbf{n}$ is the outward normal on the footprint A of the pillbox on the capsule surface enclosed by the contour ∂A. $\mathbf{t}$ is the anticlockwise unit vector tangential to the contour,$\boldsymbol{\tau}^{\mathrm{m}}$ is the two-dimensional stress tensor, $\mathbf{b}$ is the normal to the contour ∂A and ∇^{s} is the surface divergence operator.

The membrane follows the local fluid velocity which can be expressed as

$$\frac{\mathrm{d}\mathbf{x}_B}{\mathrm{d}t} = \mathbf{u}(\mathbf{x}_B) = \int_\Omega \mathbf{u}(\mathbf{x})\delta(\mathbf{x}-\mathbf{x}_B)\mathrm{d}V(\mathbf{x}), \quad \mathbf{x}_B\in\partial B, \tag{3}$$

where the last part relates the velocity at a membrane point to the field velocity in the entire domain Ω. The terms involving delta function in (1) and (3) anticipate the front tracking implementation.

2.2. Membrane forces

The elastic stress in the membrane is determined by the initial membrane configuration and its deformation history via two-dimensional constitutive laws. Barthès-Biesel et al. [35] compared the behavior of membranes with different hyperelastic constitutive laws, where the membrane stress–strain relations can be derived from a strain-energy function. They found that in the limit of small strain, all different constitutive relations reach a common limit of Hooke's law in terms of shear modulus G_{s} and Poisson ratio ν_{s}. At larger strains, the responses of different laws differ. Two laws (Neo-Hookean and one due to Skalak) are considered in this paper; their results are summarized below [35].

A Neo-Hookean membrane (denoted by NH below) is an example of a class of models that assume the membrane to be an infinitely thin sheet of isotropic volume-incompressible elastic media. The area of the membrane is allowed to change and its change is balanced by the thinning of the membrane. Its strain-energy function is:

$$W = \frac{G_{\mathrm{s}}}{2}\left(\lambda_1^2+\lambda_2^2+\frac{1}{\lambda_1^2\lambda_2^2}\right), \tag{4}$$

where λ_1 and λ_2 are the principal stretches on the membrane surface. The principal membrane stresses are:

$$\begin{aligned}\tau_1^{\mathrm{m}} &= \frac{1}{\lambda_2}\frac{\partial W}{\partial\lambda_1} = \frac{G_{\mathrm{s}}}{\lambda_1\lambda_2}\left(\lambda_1^2-\frac{1}{\lambda_1^2\lambda_2^2}\right), \\ \tau_2^{\mathrm{m}} &= \frac{1}{\lambda_1}\frac{\partial W}{\partial\lambda_2} = \frac{G_{\mathrm{s}}}{\lambda_1\lambda_2}\left(\lambda_2^2-\frac{1}{\lambda_1^2\lambda_2^2}\right).\end{aligned} \tag{5}$$

At large deformation, the Neo-Hookean membrane was found to display strain-softening behavior [35].

Skalak et al. [36] proposed a constitutive model for the red blood cell membrane (denoted by SK below), that incorporates area-incompressibility. The strain-energy function is given as:

$$W = \frac{G_{\mathrm{s}}}{4}\left[\left(\lambda_1^4+\lambda_2^4-2\lambda_1^2-2\lambda_2^2+2\right)+C\left(\lambda_1^2\lambda_2^2-1\right)^2\right]. \tag{6}$$

A large value of C indicates approximate area-incompressibility. The principal membrane stresses are:

$$\begin{aligned}\tau_1^{\mathrm{m}} &= \frac{G_{\mathrm{s}}}{\lambda_1\lambda_2}\left[\lambda_1^2\left(\lambda_1^2-1\right)+C\left(\lambda_1^2\lambda_2^2\right)^2\left(\lambda_1^2\lambda_2^2-1\right)\right],\\ \tau_2^{\mathrm{m}} &= \frac{G_{\mathrm{s}}}{\lambda_1\lambda_2}\left[\lambda_2^2\left(\lambda_2^2-1\right)+C\left(\lambda_1^2\lambda_2^2\right)^2\left(\lambda_1^2\lambda_2^2-1\right)\right].\end{aligned} \tag{7}$$

When C is not large, the model predicts a strain-hardening behavior [35]. From relative deformation, principal directions $\mathbf{g}_1$, $\mathbf{g}_2$ and corresponding stretches are obtained. Eqs. (5) and (7) obtain principal stresses. The stress tensor in an element then is

$$\boldsymbol{\tau}^{\mathrm{m}} = \tau_1^{\mathrm{m}}\mathbf{g}_1\otimes\mathbf{g}_1 + \tau_2^{\mathrm{m}}\mathbf{g}_2\otimes\mathbf{g}_2, \tag{8}$$

which then can be used for calculating the membrane force $\mathbf{f}^{\mathrm{m}}$ in (1). In the present formulation, we do not consider stresses due to membrane bending. This completes the mathematical description of the problem.

3. Numerical implementation

The single-fluid formulation (1) presents a system of partial differential equations with spatially varying coefficients, albeit with discontinuities and singular forces. Conventionally, the Navier–Stokes equation needs to be solved for each phase, matching boundary conditions at the interface. The front tracking method presented here treats the entire flow system as a single phase with a sharp but continuous variation of properties and forces in a finite-thickness region across the interface [3,17,19].

The entire computational domain is discretized by a 3D staggered (volume) grid. The capsule membrane described by the interface (front) is separately discretized by a triangular mesh (Fig. 1b). Smoothed representations of the properties (e.g. viscosity or density) are obtained by solving a Poisson's equation with a source that indicates the jump in the property values at the interface. The present article considers the density-matched phases. A smooth surrogate is used for the delta functions appearing in this source term as well as in (1) and (3) [37]

$$\begin{aligned}&D(\mathbf{x}-\mathbf{x}_B) = D^1(x-x_B)D^1(y-y_B)D^1(z-z_B),\\ &D^1(x-x_B) = \frac{1}{4\Delta x}\left(1+\cos\frac{\pi}{2\Delta x}(x-x_B)\right), \quad |x-x_B|\leqslant 2\Delta x.\end{aligned} \tag{9}$$

Δx is the grid spacing for the discretization. As a result, we obtain a sharply varying (over $4\Delta x$) smoothed material properties and therefore a smoothed force in (1) due to membrane once we know $\mathbf{f}^{\mathrm{m}}$. The actual representations of the singular terms in (1) and (3) become

$$\begin{aligned}&\int_{\partial B}\mathbf{f}^{\mathrm{m}}(\mathbf{x}')\delta(\mathbf{x}-\mathbf{x}')\mathrm{d}S(\mathbf{x}') = \sum_j \mathbf{f}^{\mathrm{m}}(\mathbf{x}'_j)D(\mathbf{x}-\mathbf{x}'_j)\Delta S_j,\\ &\mathbf{u}(\mathbf{x}_B) = \int_{\Omega}\mathbf{u}(\mathbf{x})\delta(\mathbf{x}-\mathbf{x}_B)\mathrm{d}V(\mathbf{x}) = \sum_i \mathbf{u}(\mathbf{x}_i)D(\mathbf{x}_i-\mathbf{x}_B)\Delta V_i.\end{aligned} \tag{10}$$

i is over all volume grid points, and j is over all surface elements.

The membrane force is computed using the deformation of the triangular element on the front from its initial undeformed configuration [33,38]. During deformation, each element remains flat and the strain is homogeneous within each element. To calculate the strain tensor for each element, we first transform (by displacement and rotation) both the undeformed and deformed elements in 3D space into the same 2D local coordinate as shown in Fig. 1d. Node 1 and node 1′, and the direction of edge 12 and 1′2′ coincide with each other. Such rigid motion does not result in any deformation. For linear triangular element, the relative displacements $\Delta\mathbf{v}$ of any point P are functions of the displacement of the ith node $\Delta\mathbf{v}_i$ as [38]:

$$\Delta\mathbf{v} = \sum_{i=1}^{3} N_i\Delta\mathbf{v}_i, \tag{11}$$

where N_i is the linearly interpolating function commonly used in finite element:

$$\begin{aligned} N_i &= \frac{a_i x + b_i y + c_i}{2A_0^{\mathrm{e}}}, \\ a_i &= y_k - y_j, \\ b_i &= x_k - x_j, \\ c_i &= x_j y_k - x_k y_j, \\ 2A_0^{\mathrm{e}} &= a_i x_i + b_i y_i + c_i, \end{aligned} \tag{12}$$

j and k terms are cyclic. The strain tensor $\mathbf{E}_{\mathrm{e}}$ therefore is:

$$\mathbf{E}_{\mathrm{e}} = \begin{bmatrix} \frac{\mathrm{d}(x+\Delta v_x)}{\mathrm{d}x} & \frac{\mathrm{d}(x+\Delta v_x)}{\mathrm{d}y} \\ \frac{\mathrm{d}(y+\Delta v_y)}{\mathrm{d}x} & \frac{\mathrm{d}(y+\Delta v_y)}{\mathrm{d}y} \end{bmatrix} = \begin{bmatrix} 1 + \frac{1}{2A_0^{\mathrm{e}}}\sum_i a_i \Delta v_{x,i} & \frac{1}{2A_0^{\mathrm{e}}}\sum_i b_i \Delta v_{x,i} \\ \frac{1}{2A_0^{\mathrm{e}}}\sum_i a_i \Delta v_{y,i} & 1 + \frac{1}{2A_0^{\mathrm{e}}}\sum_i b_i \Delta v_{y,i} \end{bmatrix}. \tag{13}$$

The principal stretches (eigenvalues) λ_1, λ_2 and their directions (eigenvectors) $\mathbf{g}_1$, $\mathbf{g}_2$ are computed for $\mathbf{E}_{\mathrm{e}}$. With the elastic media assumed to be isotropic, the principal stresses are in the same directions as the principal stretches. The principal stress components are obtained using Eqs. (5) and (7). A stress tensor is then computed for each element using Eq. (8). Elastic forces on the element edges are calculated from the stress tensor

$$\delta\mathbf{F}^{\mathrm{m}} = \int_{\mathrm{edge}} \boldsymbol{\tau}^{\mathrm{m}} \cdot \mathbf{b}\,\mathrm{d}C, \tag{14}$$

where $\mathbf{b}$ is the normal to the edge. The total force exerted on each membrane node is computed by adding the elastic forces acting on all the element edges connecting that node. Note that the implementation is applicable to membranes governed by arbitrary hyperelastic constitutive laws different from Eqs. (4) and (6) considered here.

We solve the resulting equation on a staggered grid by an operator-splitting projection finite-difference method. The first step of the two-step method finds an intermediate velocity $\mathbf{u}^*$ by

$$\frac{\rho^{n+1}\mathbf{u}^* - (\rho\mathbf{u})^n}{\Delta t} = -\nabla\cdot(\rho\mathbf{u}\mathbf{u})^n + \mathbf{F}^n + \nabla\cdot\boldsymbol{\tau}^n, \tag{15}$$

where $\boldsymbol{\tau}^n$ is the viscous stress. $\mathbf{F}^n$ the force due to membrane suitably smeared using relation such as (10). The spatial derivatives are approximated by central differences in their conservative form. The final velocity is computed using the pressure-correction step

$$\frac{\mathbf{u}^{n+1} - \mathbf{u}^*}{\Delta t} = -\frac{1}{\rho^{n+1}}\nabla p^{n+1}. \tag{16}$$

Requiring incompressibility be satisfied by the final velocity we obtain a Poisson's equation for pressure:

$$\nabla\cdot\left(\frac{1}{\rho^{n+1}}\nabla p^{n+1}\right) = \frac{1}{\Delta t}\nabla\cdot\mathbf{u}^*. \tag{17}$$

We use a multi-grid method for solving the pressure Poisson's equation.

An explicit scheme for calculating viscous term suffers from restrictions on time steps, i.e. $\Delta t < 0.125(\Delta x)^2\rho/\mu$, for low Reynolds numbers. To overcome this restriction, we treat some of the diffusive terms implicitly in alternate spatial directions (ADI). The viscous terms from Eq. (15) can be collected together as

$$\nabla\cdot\boldsymbol{\tau} = D_{xy} + D_{yz} + D_{zx} + D_{zz} + D_{yy} + D_{xx}, \tag{18}$$

where D_{xy}, D_{yz}, D_{zx} are the mixed derivatives, and are computed by an explicit scheme. D_{xx}, D_{yy}, D_{zz} are the double derivatives to be treated implicitly. We split the predictor step further and treat the diffusive terms by ADI:

$$\begin{aligned} &\frac{\rho^{n+1}\mathbf{u}^{****} - (\rho\mathbf{u})^n}{\Delta t} = -\nabla\cdot(\rho\mathbf{u}\mathbf{u})^n + \mathbf{F}^n + D_{xy}(\mathbf{u}^n) + D_{yz}(\mathbf{u}^n) + D_{zx}(\mathbf{u}^n), \\ &\rho^{n+1}\left(\frac{\mathbf{u}^{***} - \mathbf{u}^{****}}{\Delta t}\right) = D_{zz}(\mathbf{u}^{***}), \\ &\rho^{n+1}\left(\frac{\mathbf{u}^{**} - \mathbf{u}^{***}}{\Delta t}\right) = D_{yy}(\mathbf{u}^{**}), \end{aligned}$$

$$\rho^{n+1}\left(\frac{\mathbf{u}^{*}-\mathbf{u}^{**}}{\Delta t}\right)=D_{xx}(\mathbf{u}^{*}). \tag{19}$$

Each implicit equation above gives rise to a tri-diagonal system that is directly solved without iteration. The convergence of the scheme is ensured by prescribing for the intermediate velocities at the boundary as:

$$\mathbf{u}^{*}=\mathbf{u}^{**}=\mathbf{u}^{***}=\mathbf{u}^{****}=\mathbf{u}^{n+1}. \tag{20}$$

The ADI scheme increases the time step by one order of magnitude.

4. Results and discussion

We simulate the motion of a capsule in an imposed shear: imposed velocity $\mathbf{u}^{i}$ is given as:

$$u_x^i=\dot{\gamma}y, \quad u_y^i=u_z^i=0, \tag{21}$$

where $\dot{\gamma}$ is the shear rate. The capsule is initially spherical and placed at the center of the flow. The effects of non-spherical unstressed shapes are not considered in this paper. The simulations are performed in a rectangular computational domain (Fig. 2). In terms of the undeformed capsule radius R, the domain has the size of $10R \times 10R \times 5R$ with $10R$ in the velocity (x) and gradient directions (y), and $5R$ in the vorticity direction (z). Periodic boundary conditions are imposed in the velocity (x) and vorticity (z) directions, whereas wall boundary conditions are imposed in the direction of velocity gradient (y). We use a uniform grid with resolution $96 \times 96 \times 48$ for the domain and a front mesh with 10,242 nodes and 5120 elements for tracking the membrane deformation, unless otherwise specified. The ratio of an element edge to the grid spacing is 0.66 for the initial undeformed configuration which is sufficient to ensure an appropriate grid-front property transfer. The resolution of our discretization is much higher than that adopted by previous front tracking study of capsules [33]. The numerical convergence of our simulation is presented below.

The physical problem is governed by several non-dimensional groups: $Re=\rho R^2\dot{\gamma}/\mu_c$, $\varepsilon=\mu_c R\dot{\gamma}/G_s$ and $\lambda=\mu_d/\mu_c$, where subscripts "d" and "c" represent the dispersed and continuous phases, respectively. The Reynolds number Re represents the ratio of the inertial to the viscous forces and the capillary number ε the ratio of the viscous force relative to the elastic force due to membrane deformation. Ramanujan and Pozrikidis [8]

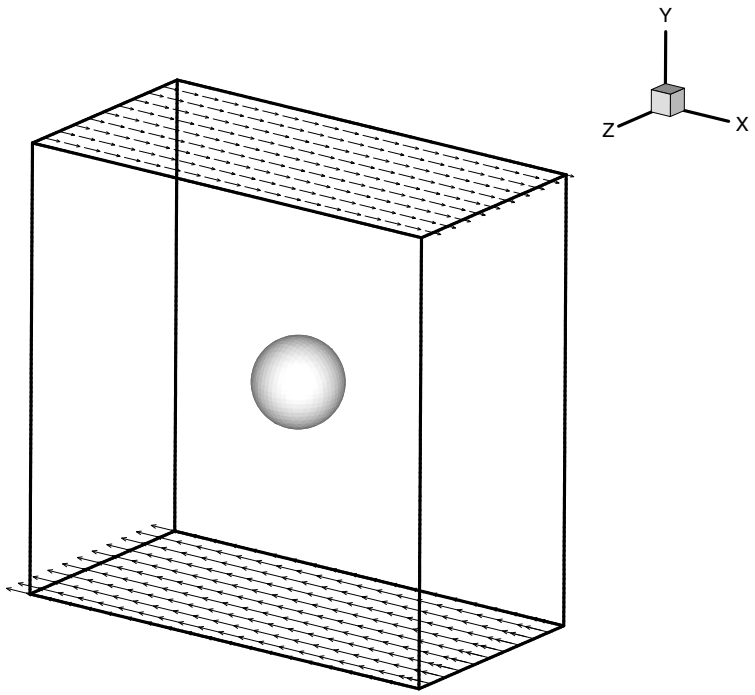

Fig. 2. Spherical capsule is deformed in an incidentally imposed shear. The simulation is performed in a rectangular box.

used Young's modulus $E_s = 3G_s$, leading to a different definition of capillary number. Note that the explicit nature of the algorithm, even though an ADI [17] implementation alleviates the restrictions on time steps, precludes achieving the Stokes limit ($Re = 0$). Our simulations are performed at $Re = 0.1$ to approximate Stokes flow. Simulation shows that ADI allows a non-dimensional time step $\dot{\gamma}\Delta t = 5e - 4$ for achieving convergence. In the following, we first evaluate the numerical accuracy of our simulation, then present and compare our simulation results for varying capillary number ε, viscosity ratio λ, and membrane constitutive laws [Eqs. (3) and (7)].

4.1. Numerical accuracy and comparison with drops

We have previously investigated the grid convergence of the front tracking method for simulating a drop in a simple shear and found that $96 \times 96 \times 48$ is sufficient for accurate description of drop dynamics [30]. The effects of finite domain size were also found to be negligible. Here we reinvestigate the convergence, for the capsule membrane introduces new forces which might influence the accuracy. In a shear flow, a spherical capsule, like a drop, transiently elongates to an approximate ellipsoidal shape and aligns itself with its largest axis forming an angle θ with respect to the flow direction (x). The deformation of the capsule in shear flow is characterized by a parameter D_{xy} given by Taylor [39,40]:

$$D_{xy} = \frac{L - B}{L + B}, \tag{22}$$

where L and B are, respectively, the lengths of the larger and smaller axes (in the x–y plane) of the ellipsoid with the same inertia tensor as the deformed capsule [8]. The inertia tensor is defined as:

$$\mathbf{I}^d = \int_V (r^2\mathbf{I} - \mathbf{xx})\mathrm{d}^3 r = \frac{1}{5}\int_{\partial V} (r^2\mathbf{xI} - \mathbf{xxx}) \cdot \mathbf{n}\,\mathrm{d}^2 r, \tag{23}$$

where $\mathbf{I}$ is the identity tensor. The relations between the eigenvalues $I^d_{L,B,W}$ of $\mathbf{I}^d$ and the major axes of the ellipsoid are:

$$L = \sqrt{\frac{5}{2\rho V}\left(I^d_B + I^d_W - I^d_L\right)},$$

$$B = \sqrt{\frac{5}{2\rho V}\left(I^d_L + I^d_W - I^d_B\right)},$$

$$W = \sqrt{\frac{5}{2\rho V}\left(I^d_L + I^d_B - I^d_W\right)}.$$

In Fig. 3a and b, evolutions of the deformation and the orientation angle (Neo-Hookean membrane $\varepsilon = 0.6$, $\lambda = 1.0$) are compared at different grid resolutions and time steps. With increasing grid resolution, the solutions converge. Considering the high computational cost at high resolution, we choose $96 \times 96 \times 48$ for most simulations. The steady state solutions attain small numerical errors: $|D^{96}_{xy} - D^{160}_{xy}|/D^{160}_{xy} = 3.9\%$, $|\theta^{96} - \theta^{160}|/\theta^{160} = 1.5\%$. Decreasing time step to one-fifth of the original does not significantly alter the solution as well: $|D^{5e-4}_{xy} - D^{1e-4}_{xy}|/D^{1e-4}_{xy} = 0.8\%$, $|\theta^{5e-4} - \theta^{1e-4}|/\theta^{1e-4} = 1.2\%$. In Fig. 3c and d, we see that increasing the size of the computational domain in x and z (periodic boundary) directions generates almost identical solutions. The wall boundary in y direction has a small effect on deformation $|D^{10R}_{xy} - D^{15R}_{xy}|/D^{15R}_{xy} = 0.4\%$ and orientation angle $|\theta^{10R} - \theta^{15R}|/\theta^{15R} = 1.4\%$. On a 3 GHz desktop computer, a $96 \times 96 \times 48$ simulation takes 3.5 s to compute one time step, whereas a $160 \times 160 \times 80$ simulation takes 17.5 s for the same.

Although dynamics of a simple drop as well as that of a capsule in shear have been extensively investigated, the difference between the two has not been compared and discussed much in the literature. We simulate a capsule with Neo-Hookean (NH) membrane at $\varepsilon = 0.5$, $\lambda = 1.0$ and a drop at $Ca = \mu_c R\dot{\gamma}/\sigma_s = 0.3333$, $\lambda = 1.0$, where σ_s is the surface tension. The values of ε and Ca are chosen such that the final deformation, and to a lesser extent final orientation angle are very similar in these two cases, although they undergo

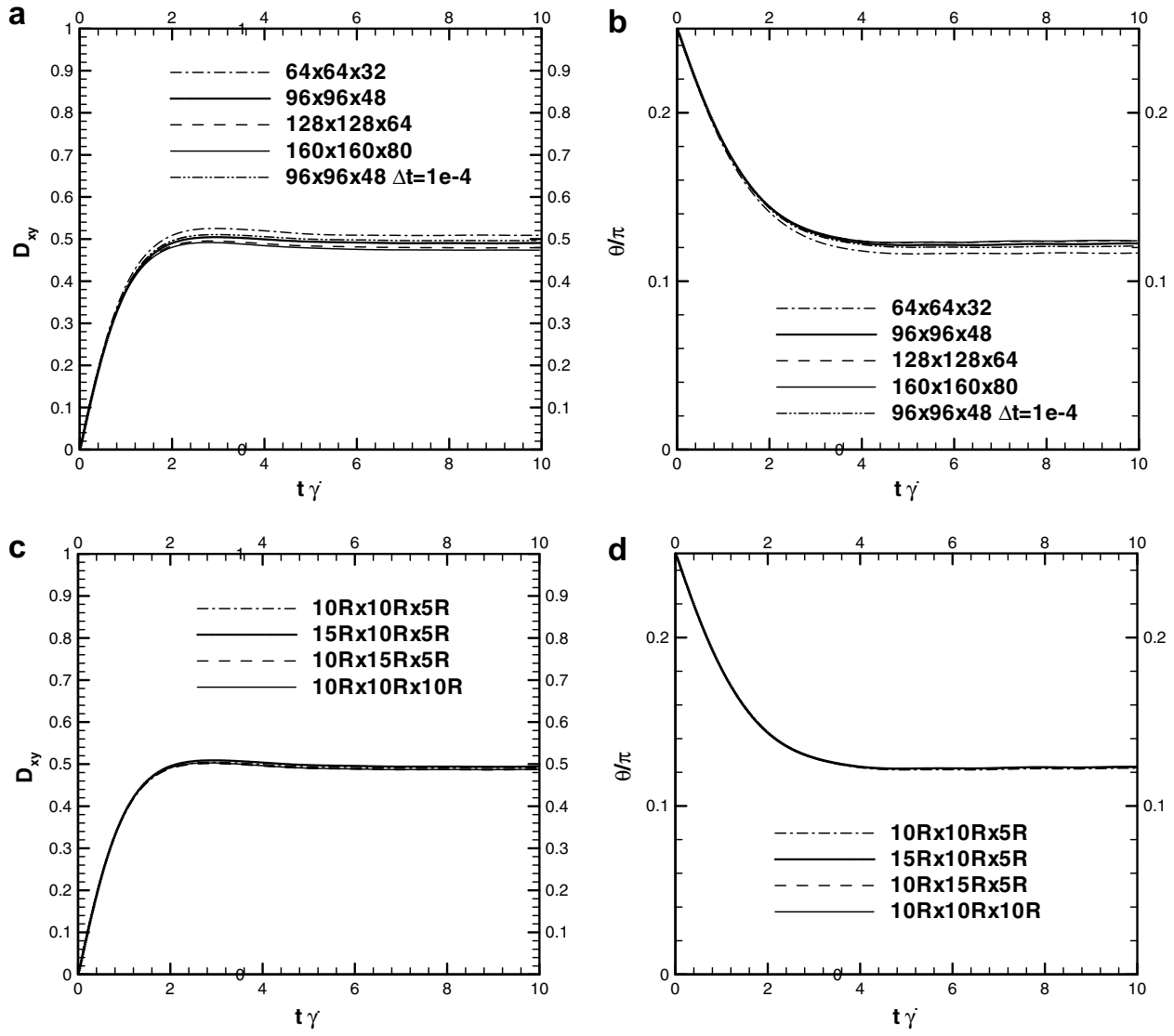

Fig. 3. Convergence of deformation and orientation angle with increasing grid resolution, decreasing time step and increasing domain size; NH membrane at $\varepsilon = 0.6$, $\lambda = 1.0$.

different transient evolution (Fig. 4a and b). However, the evolution of major axes in Fig. 4c and the shapes in Fig. 4d show drastic differences between the drop and the capsule. The surface tension on a drop has the tendency to minimize the surface area, and the stress on the surface is always tensile for any drop shape. In contrast to a drop, a capsule has an unstressed equilibrium shape. Elastic tensions or compressions develop due to relative surface deformation. In Fig. 4c, we find the axis W in the vorticity (z) direction increases to larger than the sphere radius R for the capsule but decreases to less than R for the drop. The elastic compressions (as we will see later) on the capsule surface cause the protrusion of W axis. Since the volume inside is conserved, the more protruded W axis for the capsule leads to a smaller L and B compared to the drop with similar deformation defined by Eq. (22). The pattern is clearly shown in Fig. 4e by the shapes of the capsule and the drop. Using the formula ($p = 1.6075$):

$$A \approx 4\pi\left(\frac{L^pB^p + L^pW^p + W^pB^p}{3}\right)^{\frac{1}{p}}, \tag{24}$$

we can approximates the true surface area of the ellipsoid with a relative error of $\pm 1.061\%$. In steady state, the approximated surface area of the capsule is $A/A_0 = 1.178$ and that of the drop is $A/A_0 = 1.101$. The slight

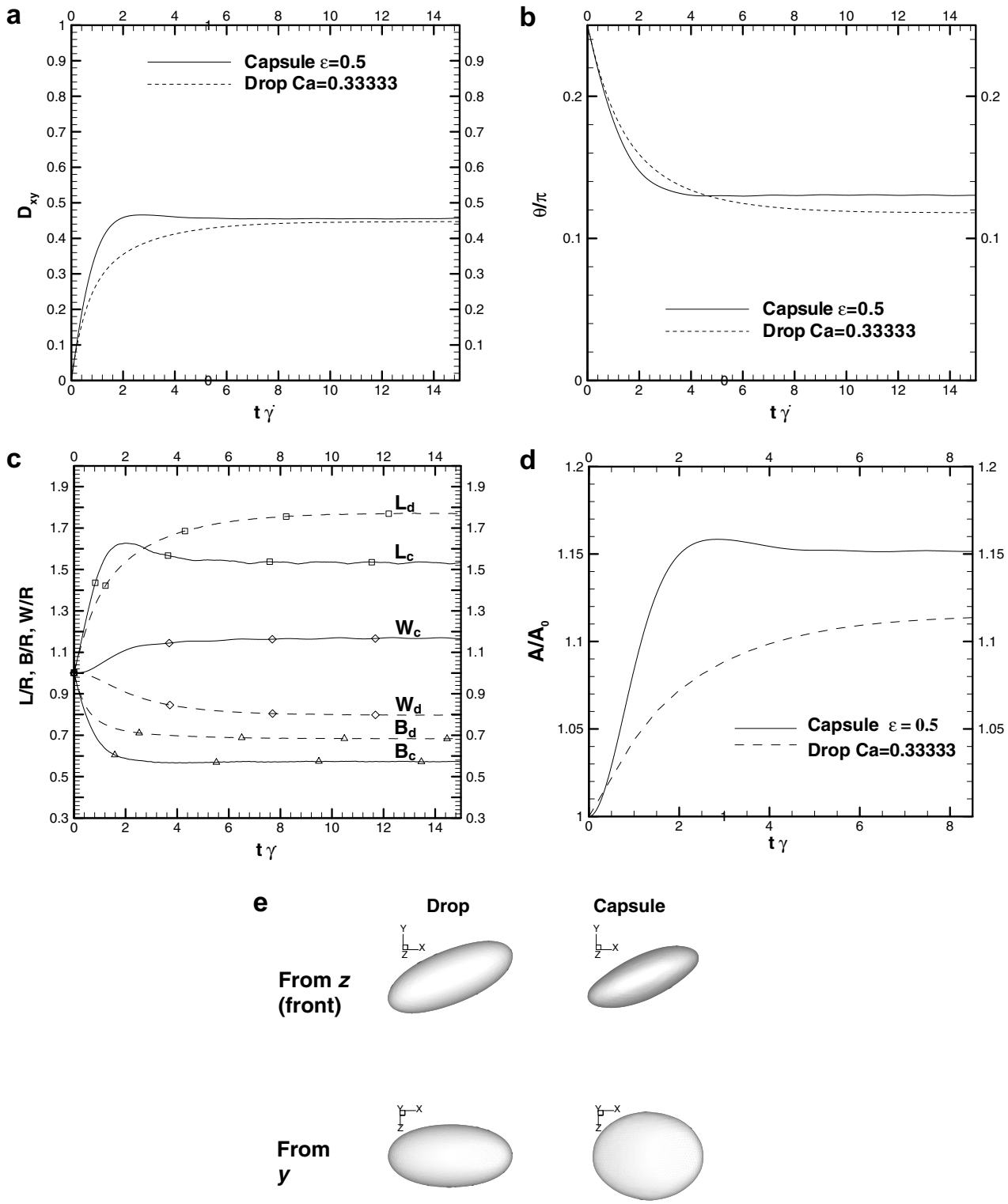

Fig. 4. Comparison of deformation (a), orientation angle (b), major axes (c) and interfacial area (d) between a NH capsule at $\varepsilon = 0.6$, $\lambda = 1.0$ and a drop at $Ca = 0.3333$, $\lambda = 1.0$ in shear; the subscript "c" and "d" in plot (c) indicate "capsule" and "drop", respectively; plot (e) compares the shapes of the drop and the capsule in different orientations at $\dot{\gamma}t = 10$.

increase of surface area of the capsule compared to the drop is confirmed by the calculation (Fig. 4d) using the simulated shapes. This observation demonstrates the severe limitation of two dimensional studies of capsules, important as they are in identifying some of the underlying physics at a considerably lower computational cost.

4.2. Deformation, orientation and tank-treading: comparison with BEM

We present a systematic comparison of front tracking and other methods in predicting capsule deformation, orientation and tank-treading behavior. The membrane constitutive law and the viscosity ratio are varied. Our simulation results are compared with the first-order analytical perturbation theory by Barthès-Biesel [1] and Barthès-Biesel and Rallison [2] (represented by Analytic BB in the figures) and BEM simulation by Lac et al. [10] (represented by BEM LBPT in the figures) and by Ramanujan and Pozrikidis [8] (represented by BEM RP in the figures).

In Fig. 5a, the transient deformation for Neo-Hookean (NH) capsules in shear is shown at varying capillary numbers ε. At low capillary numbers $\varepsilon = 0.075$, 0.15, an equilibrium deformation is first reached, then the deformation shows a slow decrease. The decrease in deformation indicates the formation of unstable buckles due to compressive stresses developed on the capsule surface. This issue will be discussed later. To compare with previous results obtained using BEM, we define a stable deformation similarly as other groups did [7,8,10]: we consider the capsule to be stable up until the instance when the equilibrium deformation starts to decrease and call the short-period equilibrium deformation as the stable deformation, even if the capsule

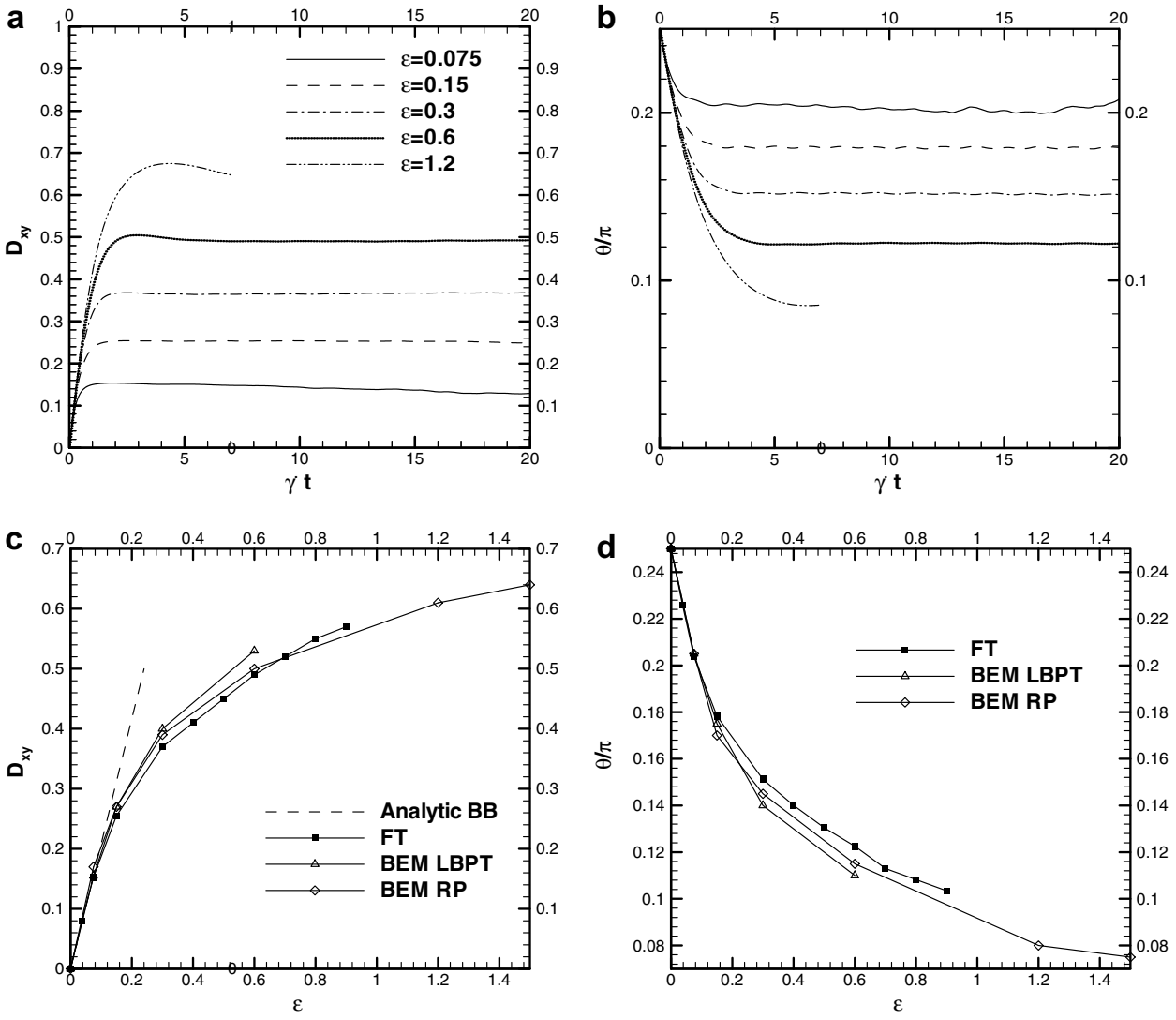

Fig. 5. Deformation (a) and orientation angle (b) vs. time for NH membrane at varying capillary numbers at $\lambda = 1.0$ (same legends for curves in (a) and (b)); (c) and (d) shows the corresponding stable deformation and orientation angle vs. capillary number, with results by different methods compared.

will become unstable afterwards. As the capillary number is increased to $\varepsilon = 0.3, 0.6$, the capsule maintains an equilibrium shape for long time after transient deformation. The stable deformation increases with increasing ε as a result of increasing viscous stretching relative to the elastic constraining force on the membrane. Further increase of the capillary number to $\varepsilon = 1.2$ leads to a transient overshoot followed by a large bounded deformation. However, our simulation could not continue for $\dot{\gamma}t > 7$ due to the numerical difficulty with high-curvature tips for highly elongated capsules.

Fig. 5b shows the evolution of orientation angle for NH capsules in shear at varying capillary numbers ε. At low capillary numbers $\varepsilon = 0.075, 0.15$, the orientation angle first reaches an equilibrium value, then displays small oscillations due to the formation of buckles. Similar to deformation, we define a stable orientation angle as the short-period equilibrium angle before the instability sets in. At intermediate capillary number $\varepsilon = 0.3, 0.6$, θ maintains a stable value for a long time. An increase in capillary number causes a decrease in θ, and the capsule becomes more aligned with the flow direction. At a high capillary number $\varepsilon = 1.2$, θ reaches an equilibrium value before the simulation stops due to numerical difficulty.

In Fig. 5c and d, we plot, respectively, the stable deformation and orientation angle as functions of capillary number and compare our simulation with other methods. The perturbation theory predicts a linear relation between deformation and capillary number in the small deformation range: $D_{xy} = 25\varepsilon/12$ and a constant orientation angle $\theta = \pi/4$. In Fig. 5c and d our simulation matches well with the analytic theory and results from BEMs. θ decreases to less than $\pi/4$ at non-zero ε. At intermediate capillary numbers ($0.15 < \varepsilon < 0.6$), $D_{xy}(\theta)$ by FT is slightly lower (higher) than BEM predictions. D_{xy} by front tracking becomes larger than that by BEM RP executed by Ramanujan and Pozrikidis because we simulated a NH membrane, which at high ε has a slightly larger deformation than that obtained by the zero-thickness shell model [8,10], even though for low values of ε they are shown to be equivalent. Lac et al. [10] used a structured mesh combined with curvilinear coordinates to discretize the membrane surface. As the authors pointed out, the simulation could not continue when the poles in the curvilinear coordinate move to the locations under compressive stress. Therefore, they were not able to capture bounded large deformations with compressive surface stress near the tips. On the other hand, Ramanujan and Pozrikidis [8] used an unstructured triangular mesh that effectively relieved the numerical instability due to singularity at the poles of the structured mesh. Therefore, they were able to simulate large capsule deformation for ε up to 3.0. We used a similar unstructured mesh and found stable large deformation for $\varepsilon \leqslant 1.0$. The lower-order stress computation compared to BEM RP executed by Ramanujan and Pozrikidis might explain the numerical difficulties in our simulation for high ε (Fig. 5a). We conclude that our simulation matches well with higher order BEM simulations in predicting stable deformation as well as orientation angles.

In Fig. 6a and b, we compare the effects of viscosity ratio – which exerts significant effects on both the deformation and the inclination angle – on a capsule with an NH membrane. At $\lambda = 0.2$, analytical results due to Barthès-Biesel matches with front tracking and BEM at small capillary numbers ($\varepsilon < 0.075$). At larger capillary numbers, front tracking and BEM match very well in predicting both deformation and orientation angle. Similar to the case of a drop [41], an increased viscosity ratio$\lambda = 5.0$ leads to an increased alignment of the capsule with the flow (compare Fig. 6b with Fig. 5c). Consequently, the capsule experiences less stretching (in a shear flow the stretching is maximum at $\theta = \pi/4$) and leads to a decreased deformation. The opposite happens for viscosity ratio lower than unity, $\lambda = 0.2$. We note that the front tracking simulation predicts a slightly larger deformation and orientation angle than BEM RP at $\lambda = 5.0$. Fig. 6c and d compares our simulation with BEM results for Skalak (SK) membrane at varying C. Larger C implies a larger area-dilation modulus and stronger resistance to area compression. A perturbation analysis predicts the relation between stable deformation and capillary number as $D_{xy} = (2 + 3C)\varepsilon/(1 + 2C)$. The analytical results almost overlap for $C = 1$ and 10 cases, and therefore have very limited applicability. Our simulation matches better with BEM LBPT due to Lac et al. at smaller C ($C = 1$) than at larger C ($C = 10$), implying limitation of the low-order surface stress calculation of FT in accurately modeling high area-dilation modulus. Similar numerical problems were also experienced by Eggleton and Popel while simulating red blood cells [33]. The simulation was unstable for membranes with high area-dilation modulus. Even with the high-order BEM, Lac et al. [10] observed that the numerical instability exists for $C > 10$ if the time step is not significantly decreased.

In Fig. 7, we explore the tank-treading behavior of the capsule. As the capsule reaches an equilibrium shape in the long-time limit, the normal velocity on the membrane interface vanishes while the tangential velocity

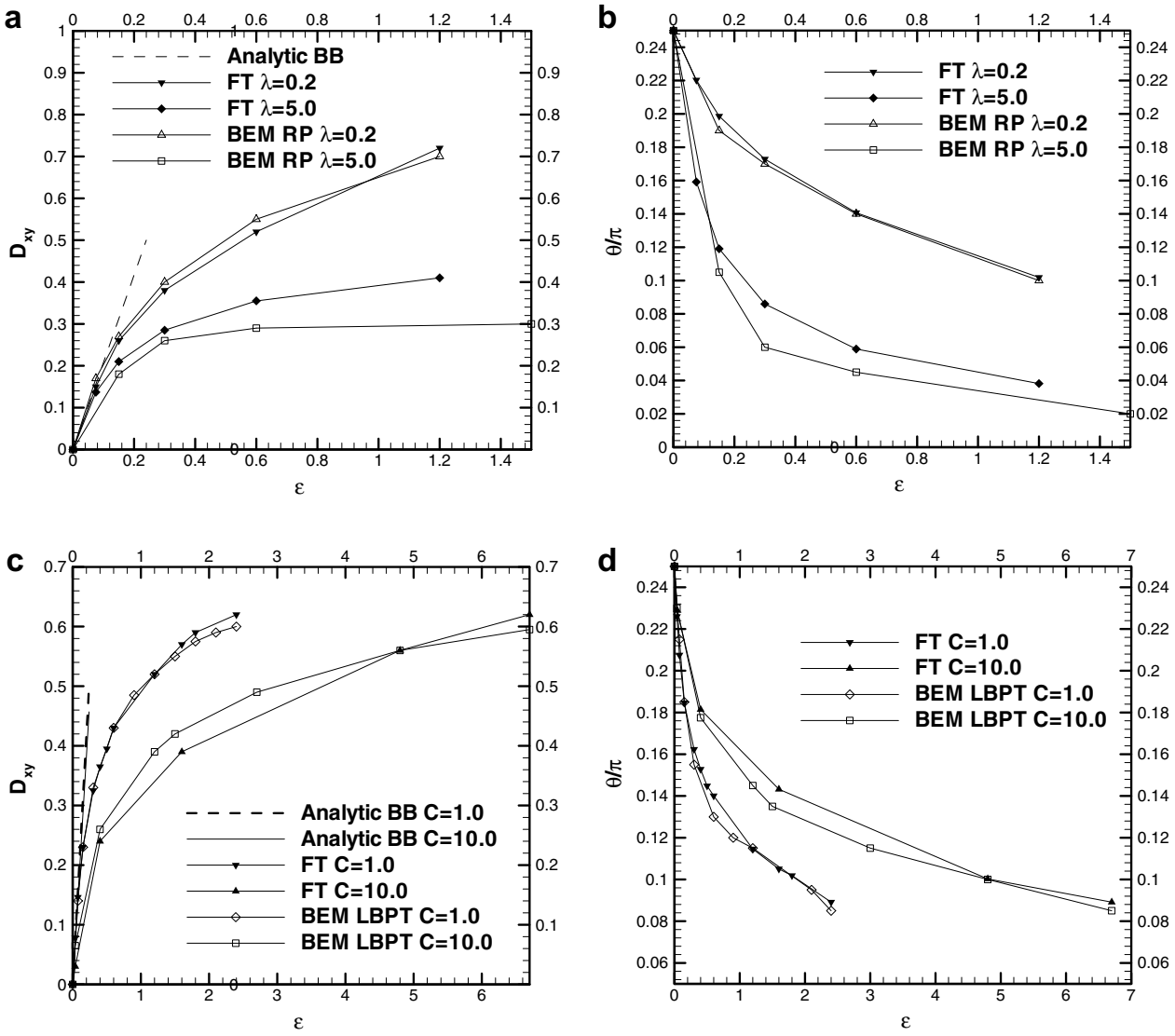

Fig. 6. Stable deformation and orientation angle vs. capillary number are shown in (a) and (b) for NH membrane at $\lambda = 0.2$, 5.0, and in (c) and (d) for SK membrane at $\lambda = 1.0$, $C = 1.0$, 10.0. Results by different methods are compared.

attains a finite value. Each membrane patch moves along a fixed circulating trajectory on the membrane surface. Such periodic motion was first identified for red blood cells in shear flow [5] and named the "tank-treading motion". Fig. 7a shows at varying ε the trajectories of interface point initially at the top of the sphere. Larger ε leads to a larger capsule deformation and a larger orbit for the interface point to circulate. It also takes a longer time for the interface point to enter the circulation orbit. As we mentioned before, the capsule at small ε forms buckles on its surface. The buckles circulate along the membrane surface as they develop. As a result, the trajectory (at $\varepsilon = 0.075$) of the interface point does not display oscillations or ripples. However, the trajectory is affected by an instability showing a deviation from the first circulating orbit in the second period. In Fig. 7b, we compare our FT simulation with other BEMs in predicting the tank-treading period ($\mathrm{TTP} = T_{\mathrm{tt}}\dot{\gamma}$). The tank-treading period is evaluated as the difference between the time when a membrane node in the center shear plane leaves a fixed point in space and the time when it returns to this point after one circulation. A slightly different way of computing it was offered by Lac et al., and was shown to be equivalent to the current procedure [10]. At $\varepsilon = 0$, the capsule rotates as a rigid sphere in shear flow with period 4π. TTP increases with increasing ε due to increased deformation and longer circulating orbits. An higher viscosity value inside the capsule retards the fluid motion inside and the motion at the membrane interface [8]. As a result, the tank-treading period increases with λ. The front tracking simulation matches other BEM

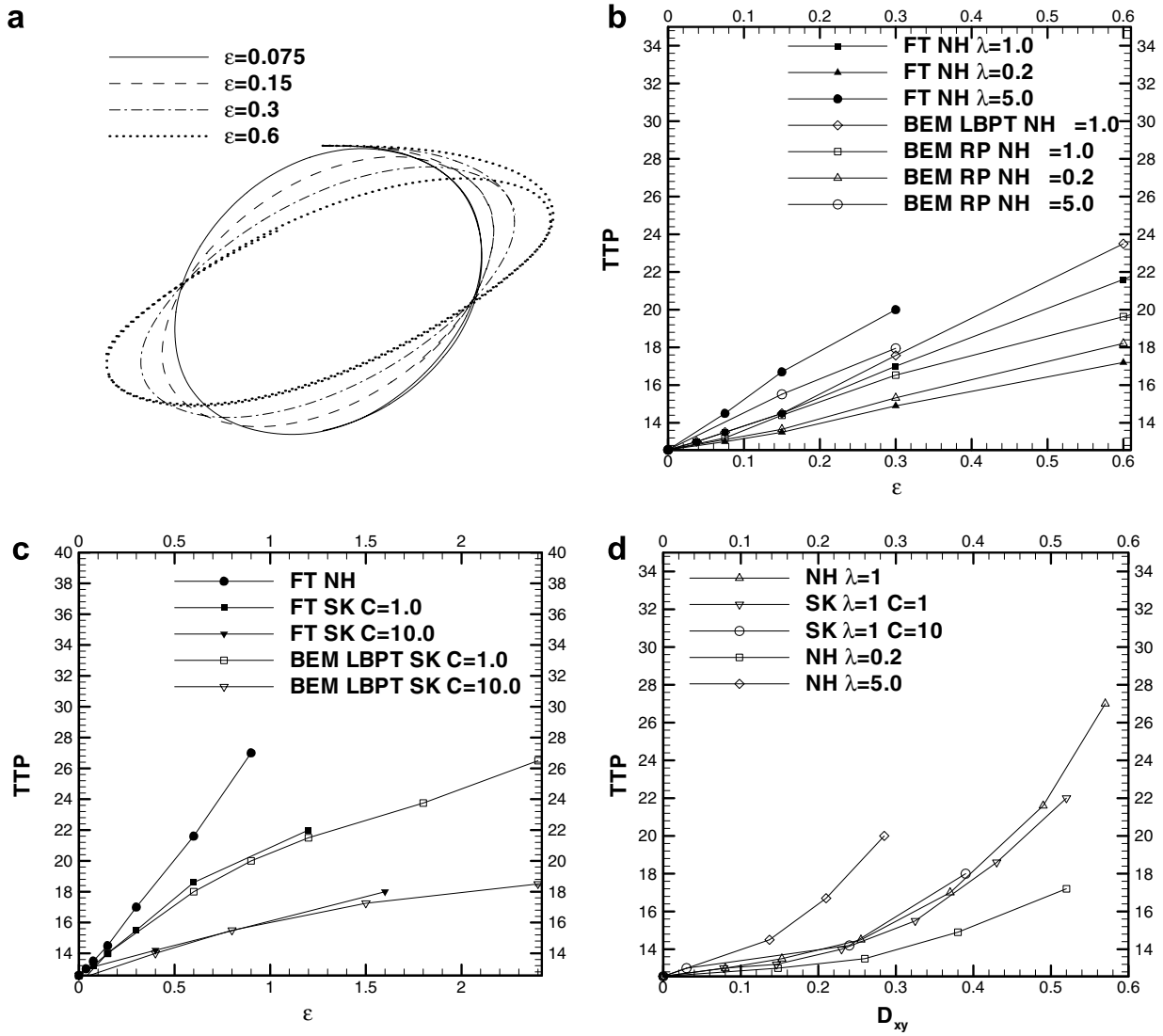

Fig. 7. (a) Trajectory of an interface point as the membrane experiences tank-treading, NH at $\lambda = 1.0$; non-dimensional tank-treading period (TTP) vs. capillary number predicted by different methods for NH in (b) and SK at $\lambda = 1.0$ in (c); TTP vs. stable deformation is shown in (d).

calculations at small ε. At large ε, two BEM computations (LBPT and RP) at $\lambda = 1.0$ predict different TTP due to the difference in numerical implementation, and extreme sensitivity of the computation. The front tracking results display the same level of variability with either result. In Fig. 7c, we report a comparison between our simulation and BEM due to Lac et al. in predicting tank-treading period for an SK membrane. Our simulation matches with the BEM in the range of ε investigated. For comparison, we also provide the case of an NH membrane, which produces the same result as an SK membrane in the limit of small ε (i.e. small deformation). Note however that the SK membrane results in a significantly decreased tank-treading period at larger ε. It is observed that larger C (larger area-dilation modulus) leads to a smaller deformation and a slower tank-treading motion (smaller TTP). In the limit of infinitely large C, the TTP would decrease to 4π, that of a rigid sphere in shear. In their BEM investigation, Lac et al. [10] also reported a one-to-one mapping between deformation and tank-treading period at $\lambda = 1.0$; the data for different membrane rheology fall on the same curve. Similar phenomena are confirmed by our simulation as shown in Fig. 7d. However, we find that the collapse is disrupted for non-unity viscosity ratios. The tank-treading period indicates the time that a fluid particle takes to traverse the deformed interface. Its increase with increased deformation at a particular viscosity ratio is a result of the longer length that the fluid particle has to traverse. On the other hand, higher

(lower) viscosity ratio retards (accelerates) the tangential velocity leading to an increase (decrease) in TTP at the same deformation.

4.3. Membrane stress and buckling instability at low capillary number

In this section, we discuss the issue of capsule instability at low capillary numbers. In their early work [1,2], Barthès-Biesel and co-workers reported a compressive stress on the membrane using an asymptotic analysis. They have recently performed a numerical investigation of its impact on the stability of a capsule [10]. They used a high-order BEM to find compressive stress on the membrane. They stated that in the absence of bending rigidity, it causes the membrane to form buckles, leading to instability like the Euler instability for elastic rods. For shear and extension and various membrane constitutive equations, they numerically identified a range of capillary numbers where the stress is tensile everywhere on the membrane, and therefore the capsule is stable. In Fig. 8, we show capsule shapes from our front tracking simulation for a Neo-Hookean (NH) membrane at $\varepsilon = 0.6$ along with the distribution of the compressive stress on the capsule surface. Lac et al. [10] reported tensile stresses everywhere on the capsule surface for the range $0.45 < \varepsilon < 0.63$ at simple shear. Note that Lac et al. utilized bi-cubic B-splines basis functions to describe surface quantities that have continuous second derivatives. The stress plotted in Fig. 8 is obtained using a lower-order calculation based on the deformations of flat elements. Take the NH membrane [Eq. (5)] for example; if numerical error causes either $\lambda_1 < \lambda_2^{-2}$ or $\lambda_1 < \lambda_2^{-0.5}$, one stress component will be negative (compressive). However, we see that the numerically computed compressive stress is restricted to a narrow band, not affecting the global solution much, as seen in the comparisons in Figs. 5–7, and the capsule remains stable without forming buckles. We note that in contrast to the simulation of Lac et al., in FT the membrane force is smeared over several grid points (about $4\Delta x$) across the membrane and therefore experiences a local averaging which may arguably relieves some of the destabilizing forces.

On the other hand, the front tracking simulation does capture the buckling instability at low capillary numbers, as seen in Fig. 9. For capillary numbers below $\varepsilon \sim 0.15$, the deformation shows a steady decline with time and eventually small oscillations occurs. For $\varepsilon = 0.075$, shapes clearly show that the decline in deformation coincides with an appearance of surface wrinkling. Since the buckles are unstable, the deformation shows small oscillations. At such a low capillary number, the compressive stress dominates on the membrane surface, as shown by the white region (in contrast to Fig. 8). The distribution of the compressive stress becomes highly irregular as the unstable buckles develop.

As pointed out by Lac et al. [10], who saw similar buckles, in the absence of bending rigidity, the simulation cannot be trusted to represent the true physics once the buckles appear and the instability sets in. We investigate this issue by comparing the grid dependence of capsule shapes (Neo-Hookean or NH membrane at $\lambda = 1.0$) with buckle formation ($\varepsilon = 0.075$) and without buckle formation ($\varepsilon = 0.6$) in Fig. 10. For the buckled capsule in Fig. 10a–c, we find higher grid resolution $160 \times 160 \times 80$ in Fig. 10b generates a smoother surface with more regular folds than $96 \times 96 \times 48$ in Fig. 10a. However, when a denser mesh with 40,962 nodes for the membrane is used in Fig. 10c, the capsule shape displays drastically different buckles from those in Fig. 10a and b. For the stable capsule with smooth surfaces in Fig. 10d–f, we find the capsule shape is independent of grid and front resolutions. Therefore, we conclude that for the case of an unstable capsule, our simulated

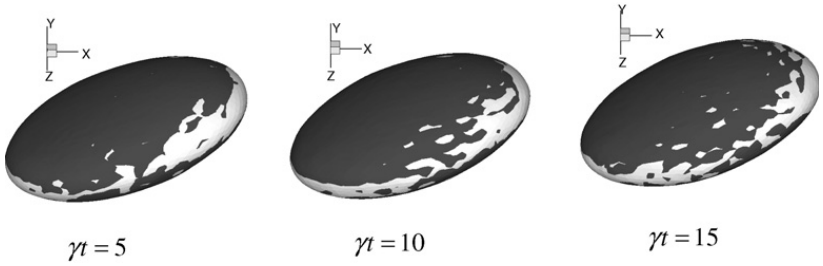

Fig. 8. The distribution of compressive stress (white region) on capsule surface at different time instants; NH membrane at $\varepsilon = 0.6$, $\lambda = 1.0$.

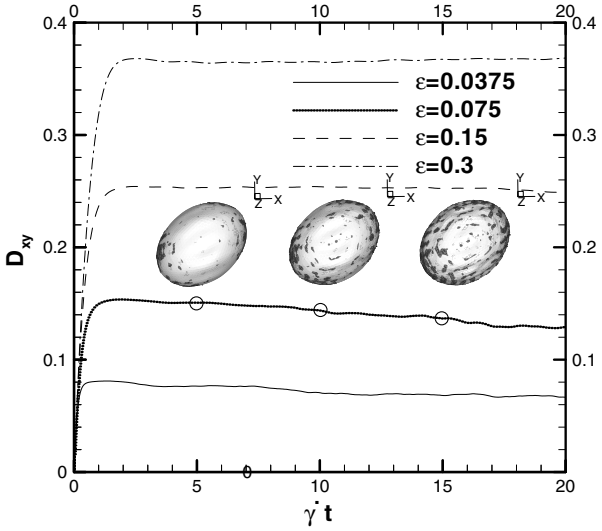

Fig. 9. Deformation vs. time for NH membrane at low capillary numbers and for $\lambda = 1.0$; inset shows the capsule shapes with developing buckles and compressive stress (white region) distribution at time instance $\dot{\gamma}t = 5$, 10, 15 for $\varepsilon = 0.075$.

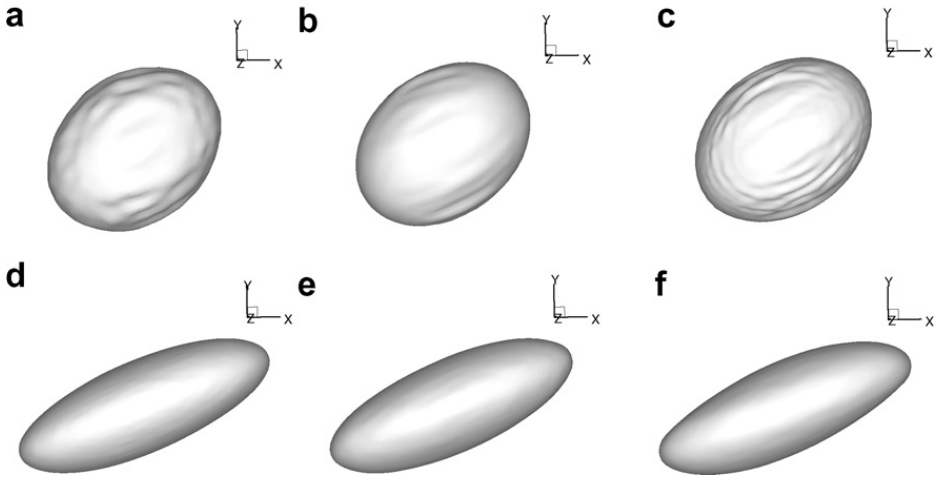

Fig. 10. Shapes of a NH capsules at $\lambda = 1.0$, $\dot{\gamma}t = 10$ are shown in (a)–(c) for $\varepsilon = 0.075$ and (d)–(f) for $\varepsilon = 0.6$; (a) and (d) are at low grid resolution $96 \times 96 \times 48$, (b) and (e) at high grid resolution $160 \times 160 \times 80$, and in (c) and (f) at high grid and front (40962 nodes) resolution.

buckles depend on resolution and do not represent true physics. Capsules in applications usually have finite thickness and a finite amount of bending rigidity. Including bending in the model will allow the simulation to capture a physical wavelength of the buckles under compressive stress [10].

We believe that the surrounding fluid flow affects the stability of capsules in presence of membrane compression. A capsule in an extensional flow deforms into a stationary state where the capsule membrane does not rotate unlike in shear flow. We believe that the tank-treading motion of membrane in a shear flow has a stabilizing effect on the membrane. Fig. 11a shows that the capsule in shear at $\varepsilon = 0.3$ and the capsule in extensional flow at $\varepsilon = 0.12$ reach similar deformation. Note that they are outside the numerically computed stable ranges ($0.45 < \varepsilon < 0.63$ for shear, $0.14 < \varepsilon < 0.21$ for extensional flow) provided by Lac et al. [10]. The planar extensional forcing flow $\mathbf{u}^i$ is defined by

$$u_x^i = \dot{\gamma}y, \quad u_y^i = \dot{\gamma}y, \quad u_z^i = 0. \tag{25}$$

The membrane stresses are computed based on the capsule deformation. Therefore, they are expected to have similar surface stress distributions for both cases in Fig. 11a. However, in Fig. 11b and c, the capsule shape in

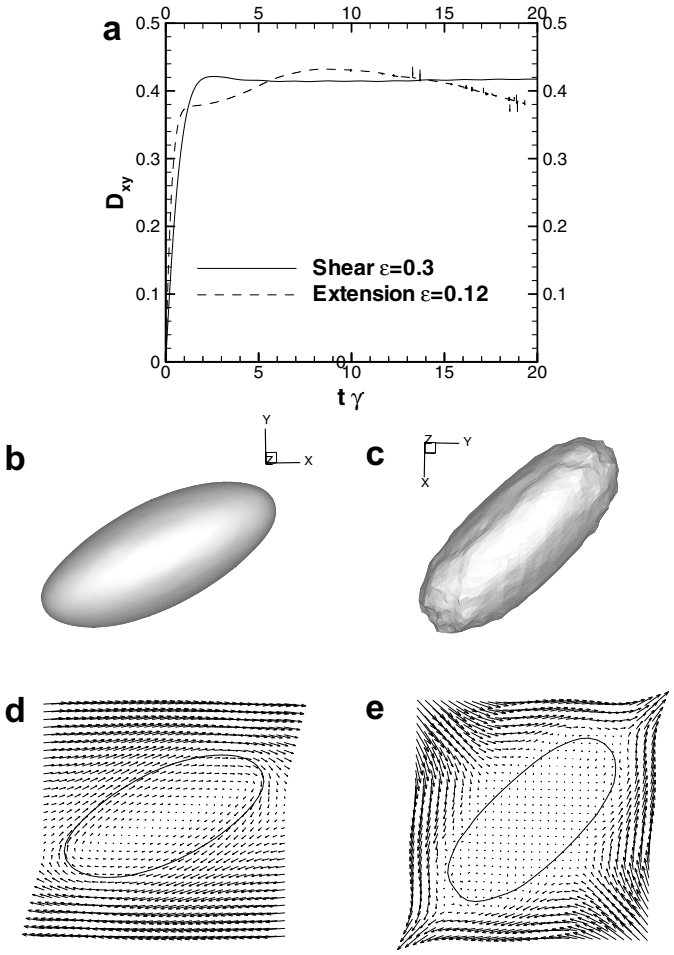

Fig. 11. (a) Comparison of the transient deformation for NH capsules at $\lambda = 1.0$ deformed to the similar magnitude in shear and extensional flow. The shapes at $\dot{\gamma}t = 10$ are shown in (b) for capsule in shear and in (c) for capsule in extensional flow. The corresponding velocity fields are shown in (d) and (e).

shear flow remains smooth while the shape in extensional flow becomes highly unstable and buckled. The lack of rotation exacerbates the effects of compressive stresses and leads to buckles and instability in the extensional flow case. The velocity fields in Fig. 11d and e clearly demonstrate the tank-treading rotation for capsule in shear flow and an almost static membrane for capsule in extensional flow. The inside fluid is static for the latter. Note that the capsule shapes in Fig. 11d and e are plotted using the smoothed indicator function of the FT formulation resulting in a smoothed contour even for a buckled capsule in extensional flow. We conclude that the tank-treading motion caused by the rotation in the imposed shear has a stabilizing effect on the capsule. The part of the membrane that undergoes compression at some time instant, is convected away to a non-compressive region of the flow, preventing buckling. The stabilizing effect of rotational part of a shear field was also noted by Lac et al. [10] to explain the stability in the initial times of a simulation when the membrane could be in compression, but only for short transient time. However, while evaluating the stability limits they stated that in the absence of bending rigidity, compressive stress on the membrane leads to buckling instability, irrespective of membrane and fluid motions. Our simulation suggests that even when a capsule is subjected to a compressive stress, and therefore is in the unstable range given by Ref. [10], as the $\varepsilon = 0.3$, $\lambda = 1.0$ shear case is, the rotation can render stable evolution. In fact, a refined discretization is seen to have no effect on the capsule for this case. In summary, we find compression however no instability in our simulation for values of parameters where Lac et al. found tension everywhere in the membrane. We also find stable solutions for values of parameters which are within the domain of instability as per their criteria. We ascribe this result to the stabilizing influence of rotation.

4.4. Large deformation and breakup at high capillary number

Finally, we investigate large deformation of a capsule at high capillary numbers. In Fig. 12a, we plot the evolution of deformation for NH capsule at $\varepsilon \geqslant 0.9$. The deformation increases with ε. As we mentioned before, further increase of capillary numbers to $\varepsilon = 1.2$ leads to a transient overshoot followed by a large bounded deformation. At $\varepsilon = 1.8$, the deformation seems to increase without bound and the simulation breaks down. However, simulation with an increased resolution continues further and indicates a bounded deformation. Pozrikidis conducted similar studies of capsules at high capillary numbers. Pozrikidis' [7] coarse-grid BEM simulation could not continue for deformations D_{xy} greater than $\sim$0.5, indicating capsule breakup. However, using higher-order BEM [8], he found that a capsule would never experience continuous elongation in a shear due to large elastic tensions developed at large deformations. Such a conclusion seems to agree with our observation of bounded deformation at high ε. A low resolution simulation as in the one presented here for $\varepsilon = 1.8$ encounters numerical difficulties due to the flow around the high-curvature tips for highly elongated capsules.

However, we note that bounded deformation by simulation does not necessarily suggest a stable shape. In Fig. 12b, the angular distribution of the smaller component of principal stresses along the surface in the x–y plane through the center of the capsule at $\varepsilon = 1.8,\ \lambda = 1,\ \dot{\gamma}t = 2.5$ is shown. The stresses for NH capsule remain positive (tensile) almost everywhere except for a narrow region around $\theta_s \approx 0.12\pi$, corresponding to the tip region (Fig. 12c). Although we contend, that the tank-treading suppresses the formation of unstable buckles, near the tips very large compressive stress might still cause the membrane to buckle. The buckles

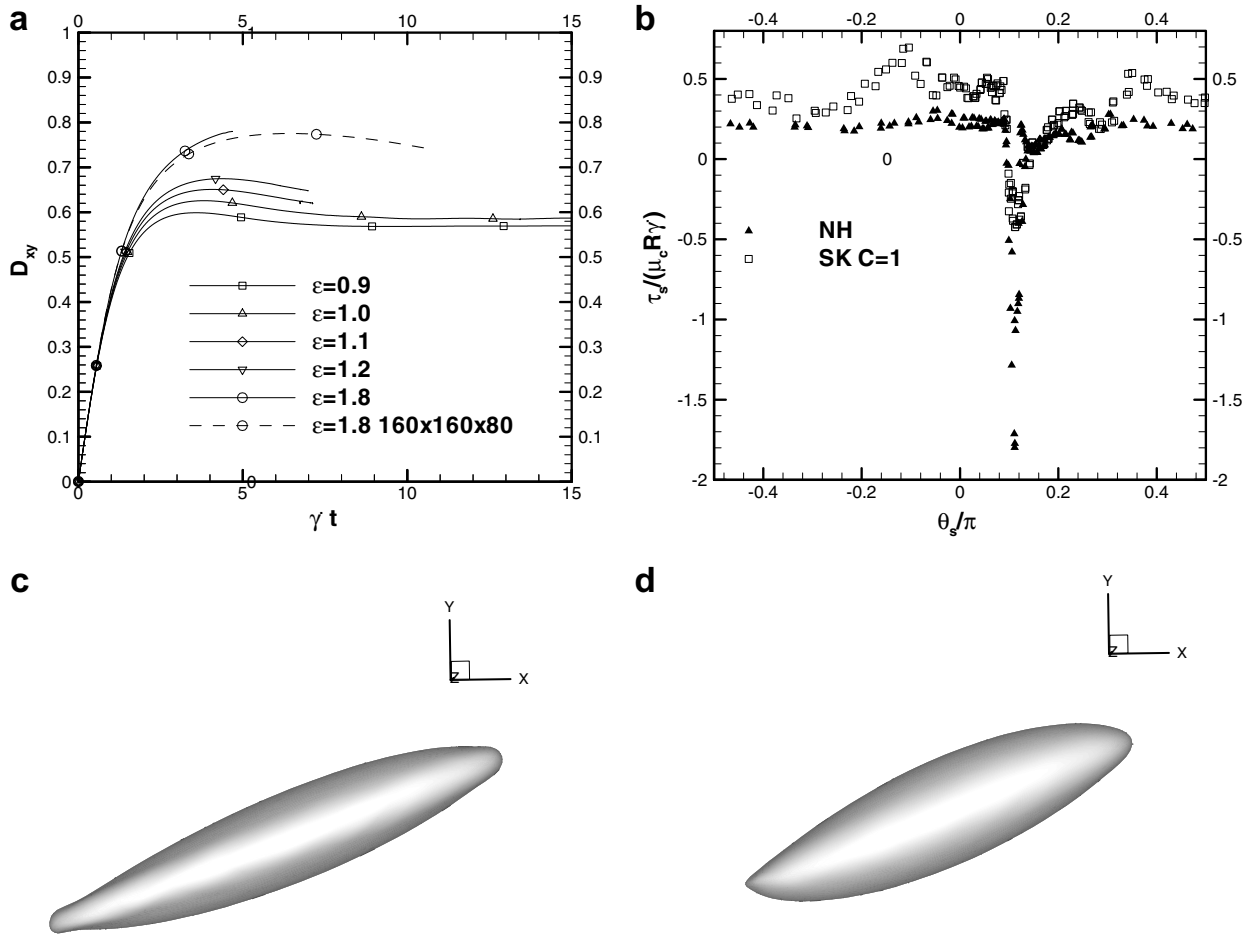

Fig. 12. (a) Deformation vs. time for capsules at high capillary numbers, NH membrane $\lambda = 1$; plot (b) shows angular distribution of the smaller component of principal stresses along the capsule surface contour in the x–y plane through the center of the capsules at $\varepsilon = 1.8,\ \lambda = 1,\ \dot{\gamma}t = 2.5$. The shapes of NH membrane (c) and SK membrane (d) are also shown.

might lead to material failure locally at the capsule tips and finally cause capsule breakup. In fact, a compressive stress has also been observed for highly deformed capsules in the BEM simulation by Ramanujan and Pozrikidis [8, Fig. 8]. Lac et al. [10] also observed compressive stress and protruded tips for capsules at high capillary number, similar to Fig. 12c. They argued that membrane compression arises from the torque exerted by the vorticity in shear flow. Based on these findings, we suggest that buckling at capsule tips can serve as a possible mechanism for capsule breakup.

Simulations by Pozrikidis [7], experiments by Chang and Olbricht [9] and the present simulation suggest multiple breakup mechanisms – membrane thinning, excessive tension and tip-buckling – all of which occurring near the capsule tip. The actual breakup of a capsule is determined by the competition of these mechanisms locally near the tip. It would be affected by the membrane rheology. To whichever aspect the resistance is weaker, the membrane is subjected to breakup by that mechanism. For example, in Fig. 12b we plot the angular distribution of principal stress for SK membrane $C = 1$ at $\varepsilon = 1.8,\ \lambda = 1,\ \dot{\gamma}t = 2.5$. It shows negative stress in the tip-region as well. However, the minimum stress is smaller than that on the NH capsule. The SK capsule therefore has a less tendency to form buckles, although it also forms protruded tips (Fig. 12d). A real capsule with a constitutive relation similar to the SK law, and with less resistance to membrane thinning or tension, would break up by these mechanisms than buckling.

5. Summary

We have simulated the deformation of a spherical capsule in shear using a front tracking method with an unstructured grid, and carefully compared its performance with that of boundary element methods. We have found that in spite of a low-order surface stress calculation, the front tracking method compares very well with high-order BEMs in predicting capsule deformation, orientation, and tank-treading motions. The unstructured grid alleviates the numerical difficulty associated with the singularity that occurs near the pole in a structured curvilinear discretization and allowed simulation where BEM based on structured grids failed. We encountered numerical difficulties for values of high ε unlike computations by Ramanujan and Pozrikidis [8]. We also predicted results different from those by Lac et al. at higher C values, indicating difficulties of our method in handling high area-dilatation modulus. We have found an interesting difference in behavior of a capsule vis-à-vis that of a drop in that for the same deformation the capsule experiences less distortion of its major and minor axes, and at the same time experiences significantly more elongation in the vorticity direction. Such an observation alerts us to the limitation of two-dimensional investigation of the capsule problem. The tank-treading period of a capsule, with different membrane constitutive laws and capillary numbers, is a function of the capsule deformation and the viscosity ratio, for these two dictates the total circumferential length a fluid particle has to travel and its tangential velocity.

We also investigate the effects of compressive stresses on membrane buckling at small and large Capillary numbers. We notice that even though the computed stress is compressive for some cases, at variance with higher order BEM computation by Lac et al., our simulation does not encounter any buckling. However, for extremely small capillary numbers, simulation does indicate buckling. In agreement with previous researchers, we also find that the buckles depend on grid resolution and hence cannot represent the true physical wavelength. A constitutive equation that includes resistance to bending is required for representing true buckling physics. We also show by simulating two cases with same deformation in shear and extension that the destabilizing effect of small compressive stress is countered by tank-treading motion in shear. The shear case investigated, although computed to be unstable by Lac et al., was found to be stable in our computation. The finding suggests that only the occurrence of compressive stress cannot be taken as a criterion for buckling instability. At high capillary numbers, the capsule was found to reach a bounded deformation with protruded tips, where unstable buckles might develop. The breakup of capsules in applications is complicated by membrane rheology locally at the capsule tips.

The excellent comparison between high-order boundary element methods and our simulation indicates that front tracking is a robust tool capable of investigating capsule problems. Its advantages primarily lie in its applicability to more complex situations such as in applications involving viscoelasticity or inertia. There boundary element, which is based on the Green's function of the linear Stokes operator, would not be available without substantial modification that would in turn lose its elegance and intrinsic advantages. Front

tracking also allows incorporation of other forces, e.g. due to chemical bonding. Such features would prove critical for biological applications, which are inherently complex in nature.

Acknowledgment

This work was supported by a Grant from National Science Foundation, CBET 0625599.

References

[1] D. Barthès-Biesel, Motion of a spherical microcapsule freely suspended in a linear shear-flow, Journal of Fluid Mechanics 100 (1980) 831–853.
[2] D. Barthès-Biesel, J.M. Rallison, The time-dependent deformation of a capsule freely suspended in a linear shear-flow, Journal of Fluid Mechanics 113 (1981) 251–267.
[3] G. Tryggvason, B. Bunner, A. Esmaeeli, D. Juric, N. Al-Rawahi, W. Tauber, J. Han, S. Nas, Y.J. Jan, A front-tracking method for the computations of multiphase flow, Journal of Computational Physics 169 (2) (2001) 708–759.
[4] M. Kraus, W. Wintz, U. Seifert, R. Lipowsky, Fluid vesicles in shear flow, Physical Review Letters 77 (17) (1996) 3685–3688.
[5] H. Schmid-Schönbein, R. Wells, Fluid drop-like transition of erythrocytes under shear, Science 165 (3890) (1969) 288.
[6] Y. Navot, Elastic membranes in viscous shear flow, Physics of Fluids 10 (8) (1998) 1819–1833.
[7] C. Pozrikidis, Finite deformation of liquid capsules enclosed by elastic membranes in simple shear-flow, Journal of Fluid Mechanics 297 (1995) 123–152.
[8] S. Ramanujan, C. Pozrikidis, Deformation of liquid capsules enclosed by elastic membranes in simple shear flow: large deformations and the effect of fluid viscosities, Journal of Fluid Mechanics 361 (1998) 117–143.
[9] K.S. Chang, W.L. Olbricht, Experimental studies of the deformation and breakup of a synthetic capsule in steady and unsteady simple shear-flow, Journal of Fluid Mechanics 250 (1993) 609–633.
[10] E. Lac, D. Barthès-Biesel, N.A. Pelekasis, J. Tsamopoulos, Spherical capsules in three-dimensional unbounded Stokes flows: effect of the membrane constitutive law and onset of buckling, Journal of Fluid Mechanics 516 (2004) 303–334.
[11] A. Diaz, N. Pelekasis, D. Barthès-Biesel, Transient response of a capsule subjected to varying flow conditions: effect of internal fluid viscosity and membrane elasticity, Physics of Fluids 12 (5) (2000) 948–957.
[12] E. Lac, D. Barthès-Biesel, Deformation of a capsule in simple shear flow: effect of membrane prestress, Physics of Fluids 17 (7) (2005) 072105.
[13] A. Walter, H. Rehage, H. Leonhard, Shear induced deformation of microcapsules: shape oscillations and membrane folding, Colloids and Surfaces A: Physicochemical and Engineering Aspects 183 (2001) 123–132.
[14] R. Scardovelli, S. Zaleski, Direct numerical simulation of free-surface and interfacial flow, Annual Review of Fluid Mechanics l31 (1999) 567–603.
[15] J.A. Sethian, P. Smereka, Level set methods for fluid interfaces, Annual Review of Fluid Mechanics 35 (2003) 341–372.
[16] D.M. Anderson, G.B. McFadden, A.A. Wheeler, Diffuse-interface methods in fluid mechanics, Annual Review of Fluid Mechanics 30 (1998) 139–165.
[17] X.Y. Li, K. Sarkar, Drop dynamics in an oscillating extensional flow at finite Reynolds numbers, Physics of Fluids 17 (2) (2005) 027103.
[18] X.Y. Li, K. Sarkar, Drop deformation and breakup in a vortex at finite inertia, Journal of Fluid Mechanics 564 (2006) 1–23.
[19] K. Sarkar, W.R. Schowalter, Deformation of a two-dimensional drop at non-zero Reynolds number in time-periodic extensional flows: numerical simulation, Journal of Fluid Mechanics 436 (2001) 177–206.
[20] Y.Y. Renardy, V. Cristini, Effect of inertia on drop breakup under shear, Physics of Fluids 13 (1) (2001) 7–13.
[21] Y.Y. Renardy, V. Cristini, Scalings for fragments produced from drop breakup in shear flow with inertia, Physics of Fluids 13 (8) (2001) 2161–2164.
[22] N. Aggarwal, K. Sarkar, Deformation and breakup of a viscoelastic drop in a Newtonian matrix under steady shear, Journal of Fluid Mechanics 584 (2007) 1–21.
[23] N. Aggarwal, K. Sarkar, Effects of matrix viscoelasticity on viscous and viscoelastic drop deformation in a steady shear flow, Journal of Fluid Mechanics (2008), in press.
[24] T. Chinyoka, Y.Y. Renardy, A. Renardy, D.B. Khismatullin, Two-dimensional study of drop deformation under simple shear for Oldroyd-B liquids, Journal of Non-Newtonian Fluid Mechanics 130 (1) (2005) 45–56.
[25] K. Sarkar, W.R. Schowalter, Deformation of a two-dimensional viscoelastic drop at non-zero Reynolds number in time-periodic extensional flows, Journal of Non-Newtonian Fluid Mechanics 95 (2-3) (2000) 315–342.
[26] P. Yue, J.J. Feng, C. Liu, J. Shen, Transient drop deformation upon startup of shear in viscoelastic fluids, Physics of Fluids 17 (12) (2005) 123101.
[27] P.T. Yue, J.J. Feng, C. Liu, J. Shen, Diffuse-interface simulations of drop coalescence and retraction in viscoelastic fluids, Journal of Non-Newtonian Fluid Mechanics 129 (3) (2005) 163–176.
[28] P.T. Yue, J.J. Feng, C. Liu, J. Shen, Viscoelastic effects on drop deformation in steady shear, Journal of Fluid Mechanics 540 (2005) 427–437.
[29] N. Aggarwal, K. Sarkar, Rheology of an emulsion of viscoelastic drops in steady shear, Journal of Non-Newtonian Fluid Mechanics 150 (2008) 19–31.

[30] X.Y. Li, K. Sarkar, Effects of inertia on the rheology of a dilute emulsion of drops in shear, Journal of Rheology 49 (6) (2005) 1377–1394.
[31] X.Y. Li, K. Sarkar, Negative normal stress elasticity of emulsions of viscous drops at finite inertia, Physical Review Letters 95 (25) (2005) 256001.
[32] X.Y. Li, K. Sarkar, Numerical investigation of the rheology of a dilute emulsion of drops in an oscillating extensional flow, Journal of Non-Newtonian Fluid Mechanics 128 (2–3) (2005) 71–82.
[33] C.D. Eggleton, A.S. Popel, Large deformation of red blood cell ghosts in a simple shear flow, Physics of Fluids 10 (8) (1998) 1834–1845.
[34] P. Bagchi, P.C. Johnson, A.S. Popel, Computational fluid dynamic simulation of aggregation of deformable cells in a shear flow, Journal of Biomechanical Engineering: Transactions of the ASME 127 (7) (2005) 1070–1080.
[35] D. Barthès-Biesel, A. Diaz, E. Dhenin, Effect of constitutive laws for two-dimensional membranes on flow-induced capsule deformation, Journal of Fluid Mechanics 460 (2002) 211–222.
[36] R. Skalak, A. Tozeren, R.P. Zarda, S. Chien, Strain energy function of red blood-cell membranes, Biophysical Journal 13 (3) (1973) 245–280.
[37] C.S. Peskin, Numerical-analysis of blood-flow in heart, Journal of Computational Physics 25 (3) (1977) 220–252.
[38] S. Shrivastava, J. Tang, Large deformation finite-element analysis of nonlinear viscoelastic membranes with reference to thermoforming, Journal of Strain Analysis for Engineering Design 28 (1) (1993) 31–51.
[39] G.I. Taylor, The formation of emulsions in definable fields of flow, Proceedings of the Royal Society of London Series A: Mathematical and Physical Sciences 146 (A858) (1934) 0501–0523.
[40] G.I. Taylor, The viscosity of a fluid containing small drops of another fluid, Proceedings of the Royal Society of London Series A: Containing Papers of a Mathematical and Physical Character 138 (834) (1932) 41–48.
[41] J.M. Rallison, The deformation of small viscous drops and bubbles in shear flows, Annual Review of Fluid Mechanics 16 (1984) 45–66.